



80 K cryogenic stage for ice lithography

Haque, Rubaiyet I.; Waafi, Affan K.; Jaemin, Kim; Briand, Danick; Han, Anpan

Published in:
Micro and Nano Engineering

Link to article, DOI:
[10.1016/j.mne.2021.100101](https://doi.org/10.1016/j.mne.2021.100101)

Publication date:
2022

Document Version
Publisher's PDF, also known as Version of record

[Link back to DTU Orbit](#)

Citation (APA):
Haque, R. I., Waafi, A. K., Jaemin, K., Briand, D., & Han, A. (2022). 80 K cryogenic stage for ice lithography. *Micro and Nano Engineering*, 14, Article 100101. <https://doi.org/10.1016/j.mne.2021.100101>

General rights

Copyright and moral rights for the publications made accessible in the public portal are retained by the authors and/or other copyright owners and it is a condition of accessing publications that users recognise and abide by the legal requirements associated with these rights.

- Users may download and print one copy of any publication from the public portal for the purpose of private study or research.
- You may not further distribute the material or use it for any profit-making activity or commercial gain
- You may freely distribute the URL identifying the publication in the public portal

If you believe that this document breaches copyright please contact us providing details, and we will remove access to the work immediately and investigate your claim.



Research paper

80 K cryogenic stage for ice lithography

Rubaiyet I. Haque^{a,*}, Affan K. Waafi^a, Kim Jaemin^b, Danick Briand^b, Anpan Han^{a,*}^a Technical University of Denmark, Department of Mechanical Engineering, 2800 Lyngby, Denmark^b Ecole Polytechnique Fédérale de Lausanne, Soft Transducers Laboratory, Neuchâtel, Switzerland

ARTICLE INFO

Keywords:

Electron beam lithography
Ice lithography
Cryostage

ABSTRACT

We present a cryogenic system design and development for ice lithography. The cryo-stage is designed with embedded channels to allow direct liquid nitrogen flow, enabling fast cryogenic cooling, and low sample temperature. The stage cools down to 78.8 K in 20 min and heats up to room temperature in 15 min, which increases throughput significantly. Compared to the previous designs, the new system reduces cooling time by 85%, and it is 50 K colder. The cryo-stage is fabricated using copper, aluminum, and polyether ether ketone (PEEK) polymer. Numerical simulations show that the thermal stress on the cryo-stage during the cooling process remains well below stage materials' mechanical yield limits. Finally, the lower stage temperature enables us to explore new precursors, materials, and applications, which we demonstrate by combining ice lithography with printed flexible electronics technology.

1. Introduction

With the advancement of nanotechnology and three-dimensional (3D) micro-and nano-scale manufacturing, several interdisciplinary fields, like, nanophotonics, electronics and biomedical engineering, have adopted them [1–4]. In the last 10 years, fluidic forced microscopy [5–7], two-photon stereolithography [8–11], focused electron beam induced deposition (FEBID) [12–15] have emerged as bottom-up additive manufacturing methods for the development of 3D micro- and nanostructures. Supplementing the above technologies, ice lithography (IL) has emerged as an efficient micro- and nano-scale direct-write additive manufacturing method [16–26].

IL applies electron-solid interaction principles to create patterns for nanodevice fabrication [17,27]. The IL process uses water and other organic precursors and can be implemented on various substrates. The IL process composes condensing precursor gases on the substrate held at cryogenic temperature and vacuum, as illustrated in Fig. 1, then exposes the ice resist by high energy focused electron beam (e-beam) for patterning. As a result, cross-linking creates a large molecule network that is stable at room temperature. Layer-by-layer processing allows the fabrication of 3D structures. Finally, excess materials are removed by the final thermal sublimation step.

A wide range of materials can be patterned using IL, assessing the forming of ice resist at cryogenic temperatures [18,21,27,28]. For example, dielectric poly(ethylene) like materials can be deposited using

alkane ice resist, such as, octane (C₈H₁₈) and nonane (C₉H₂₀). Furthermore, based on evidence from FEBID research, organometallic precursors designed for chemical vapor deposition might be employed with IL. Examples are silver (Ag), gold (Au), platinum (Pt), iron (Fe), tungsten (W), cobalt (Co), and ferrocobalt (Co₃Fe) alloys [12,29–31].

The IL method provides 1000 times higher throughput compared to FEBID [21]. Due to its ability to produce fine features of different materials in fewer steps, IL is a suitable technology for developing micro- and nano-scale 2D and 3D smart electronic devices for many applications [32]. A critical part of IL technology is the cryostage, which keeps the sample cold. The previous cryostage designs used the thermal conduction method to cool down the stage [19,27]. A flexible copper braid is employed to connect the cryogenic stage to the cold finger, which is mechanically clamped to copper rod feedthrough. The ambient end of the copper rod is dipped into a liquid nitrogen (LN₂) flask. The minimum stage temperature of 130 K can be achieved using this stage design. However, it requires relatively long cooling and heating times. What is more important, exploring new materials and precursors require lower stage temperature. Therefore, to enhance the capability and throughput of IL, we need to improve the cryogenic stage design that enables fast and better cooling and heating.

Herein, we report a new IL cryogenic stage (cryo-stage) that is compatible with smaller and modern scanning electron microscopes (SEM). Among the most important requirements are lower temperature, higher throughput, faster cooling and heating. In addition, we need to

* Corresponding authors.

E-mail addresses: rifha@mek.dtu.dk (R.I. Haque), anph@mek.dtu.dk (A. Han).

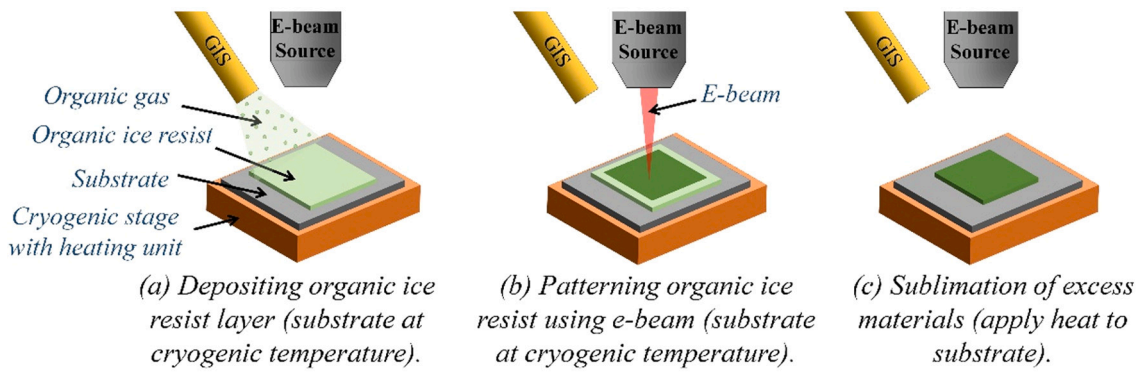


Fig. 1. Schematic of ice lithography process: (a) deposition of organic ice resist layer at cryogenic temperature, (b) pattern of the ice resist using an electron beam, and (c) sublimation of excess materials by applying heat.

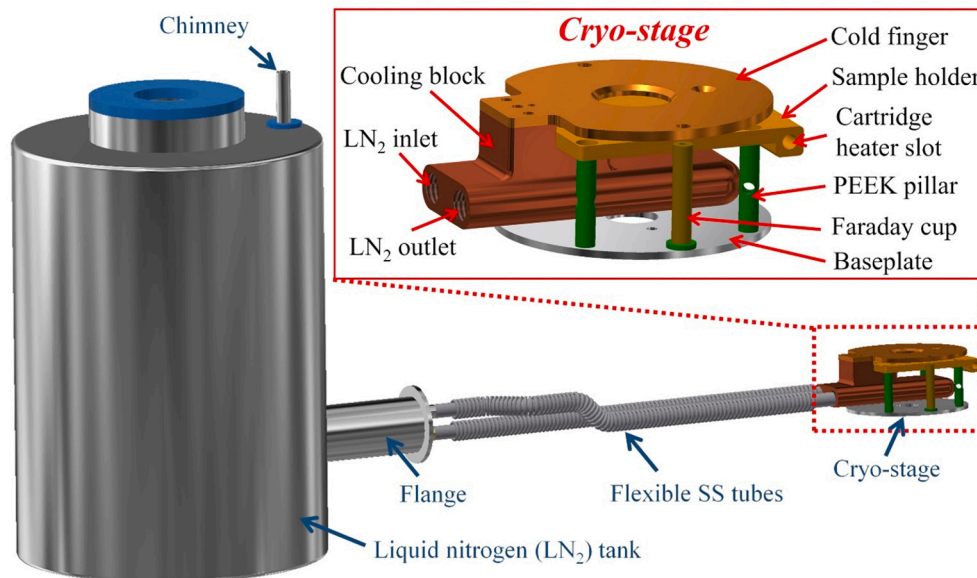


Fig. 2. Schematic diagram of the cryogenic system and cryo-stage for ice lithography.

minimize vacuum contamination by maximizing cryogenic shielding to eliminate condensable vapors in the immediate environment of the cold sample. This new cryo-stage will enable the investigation of new organic materials for IL.

2. Cryogenic stage design

The new IL cryogenic stage is compatible with the FlexSEM1000 from Hitachi. Fig. 2 illustrates the schematic of the cryogenic system design. The cryogenic system consists of external LN₂ tank mounted on the SEM vacuum chamber using a custom feedthrough flange, and the cryo-stage connected to the LN₂ tank via flexible stainless steel (SS) tubes. To enhance throughput, the new cryo-stage design is adopted for direct liquid nitrogen cooling. The cryo-stage includes a cooling block that houses a built-in channel to facilitate the LN₂ flow through the block and inlet and outlet for the LN₂, sample holder, cold-finger to minimize the vacuum contamination, and faraday cup for e-beam current measurement. The inlet and outlet of the cooling block are connected to the LN₂ tank outlet and chimney, respectively. Both the sample holder and the cold finger are connected mechanically to the cooling block. The spacing between the sample holder and the cold finger is 2.5 mm. The sample holder has an area of 40 mm × 40 mm, and an integrated cartridge heater. The cold finger outer diameter is 55 mm, and the thickness is 2 mm. To reduce heat transfer to other sections of the cryo-stage and

the SEM stage, the sample holder, the cooling block, and the cold finger are suspended on the baseplate using four thermally insulating poly-ether ether ketone (PEEK) polymer pillars. The Faraday cup for e-beam current measurement is also mounted on the baseplate.

3. Results and discussions

3.1. Thermomechanical modeling

The thermal stress due to the cooling and heating of the cryo-stage was a concern. Thus, the cryo-stage finite element (FEM) model is developed to perform numerical simulation using Comsol multiphysics software (version 5.5). Fig. 3a presents domains of the 3D model of the cryo-stage with finite element mesh. Cryogenic temperature source is introduced to the embedded channel walls. The resulting FEM model with fully coupled solid mechanics and heat transfer in the solids physics interface was solved by applying the time dependent study for 0 to 300 min.

The numerical study shows that while heating and cooling, the new design of the cryo-stage enables fast and effective heat transfer from the cooling block to the sample holder and the cold finger. Fig. 3b presents the temperature profile of the cryo-stage after 60 min of cooling. It shows the cold cooling block, sample holder, and cold finger. The baseplate did not cool to cryogenic temperature. The sample holder

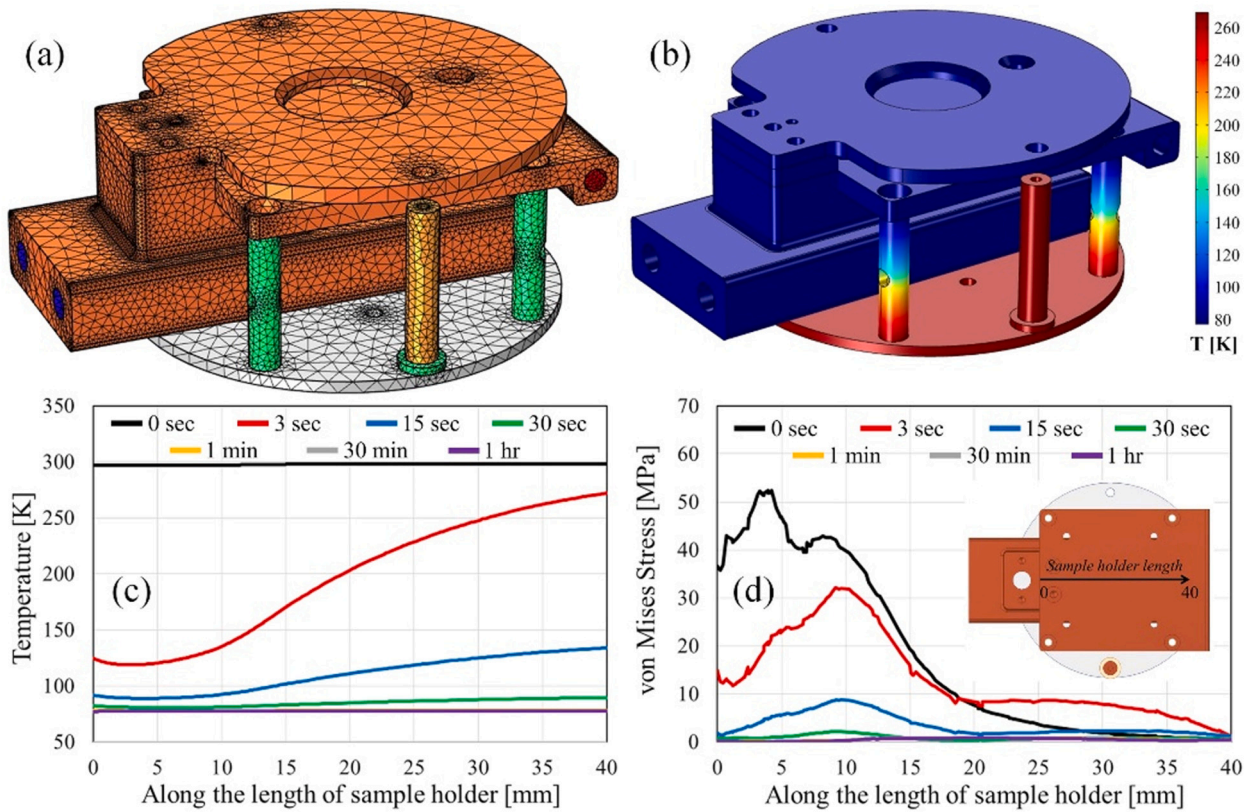


Fig. 3. Numerical simulations: (a) 3D model of cryo-stage with FEM mesh, (b) temperature profile of the cryo-stage due to heat transfer after 60 min, (c) temperature and (d) von Mises Stress along the length (representing distance from the cooling block) of the sample holder.

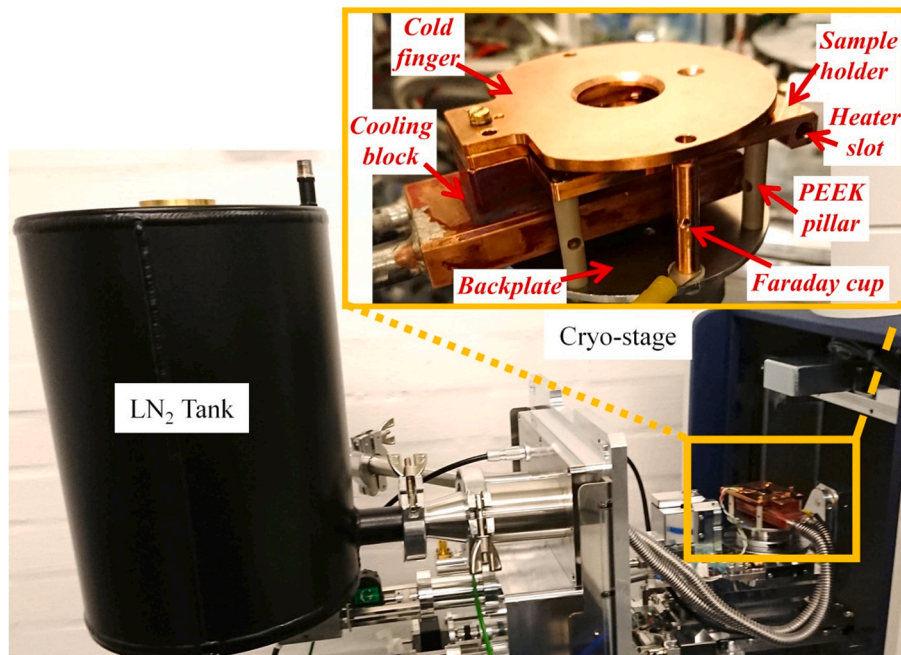


Fig. 4. Photograph of the developed (a) full cryogenic system and (b) cryo-stage. Scale: the outer diameter of the cold finger is 55 mm.

temperature evolution along its length is presented in Fig. 3c. In the ideal condition, the new design allows the sample holder to reach a uniform temperature of 77.4 K within minutes. However, because of the boiling and finite supply of LN₂, we anticipate that the experimental cooling time is significantly longer than a few minutes.

The thermal expansion and contraction due to abrupt change of temperature induce thermal stress on the cryo-stage. Fig. 3d illustrates the von Mises stress (σ_v), that refers to the equivalent stress combining three principal stress [33], of the sample holder due to cooling. Thermal stress increase for higher temperature gradient and gradually decrease

Table 1
Comparison with old [27] design.

Parameters	Old stage	This work
Stage minimum temperature [K]	130	78.8
Cold-finger minimum temperature [K]	110	81.4
Baseplate minimum temperature [K]	288	280.7
Cooling time [mins]	>120	<20
Heating time [mins]	–	<15
Vibration [nm]	30	180 ± 30

as sample holder reach homogenous and stable temperatures. The maximum thermal stress of ~ 55 MPa is observed along the length of the cryo-stage sample holder, which remains much lower than the materials yield stress (The Young modulus of copper (Cu), aluminum (Al), and PEEK is 110, 70, and 3.6 GPa, respectively). Therefore, from the numerical simulation, we conclude that the new design and the selection of materials enable fast cryogenic cooling without causing mechanical failure.

3.2. Fabrication and assembly

Fig. 4 shows photographs of the new cryogenic system and cryo-stage. The double-layered liquid nitrogen tank is designed and made in collaboration with the Kadel Engineering, Indiana, USA. Flexible SS tubes are purchased from Swagelok. Cryo-stage custom parts are made in the department machine workshop. The cooling block, sample holder, and cold-finger of the cryo-stage are made of Cu, as it has a superior thermal conductivity of 400 W/mK. The thermally insulating pillars are made of PEEK, which has a low thermal conductivity of 0.25 W/mK, and the baseplate is Al. Stainless steel flexible tubes were welded to the inlet and outlet of the LN₂ tank. The other ends of the tubes were soldered to the inlet and outlet of the cryo-stage cooling block. The cryogenic cooling system is then leak tested to confirm the integrity of the welding and soldering. The temperature measurements of the sample holder, baseplate, and the cold finger are performed using type k thermocouples. Both the thermocouple and the heater are connected to a custom-built temperature control unit that includes PID temperature controllers (model: 2216E, from EuroTherm) and power supplies. The Faraday cup is also made of Cu, with a 200 μ m Cu aperture on the top and a PEEK spacer on the bottom for electrical insulation. It is connected to the built-in picoammeter of the SEM for e-beam current measurement. The assembled cryogenic system is connected to the SEM vacuum chamber and tested. Once the cryogenic system is connected to the vacuum chamber of the SEM, the pressure is maintained below 2.5×10^{-5} mbar.

3.3. Characterization and testing

The performance of the cryo-stage is carefully tested, and the results are compared to previous IL cryostage designs [19,27] and summarized in Table 1. To assist these tests, a dedicated silicon substrate, having thin silicon dioxide coating and with Mo electrodes made by photolithography and lift-off, is placed on the sample holder of the cryo-stage. SEM vacuum is applied and the LN₂ tank is filled with liquid nitrogen. The LN₂ flows from the tank to the cooling block of the cryo-stage due to gravity. The heat transfer occurs between the LN₂ and the cooling block, and the warmer nitrogen gas escapes through the chimney. Fig. 5a shows the temperature drops with respect to time of different sections of the cryo-stage. The sample holder cooled to 78.8 K in less than 20 min. The temperature of the cold finger is 81.4 K, which allows efficient trapping of undesired condensable gasses. The temperature of the baseplate is recorded to 280.7 K after 20 min. As a result, the temperature drop does not impact the SEM stage parts, although the cryo-stage remains at cryogenic temperature. Therefore, the design of the PEEK pillars provides good thermal insulation along with mechanical stability and robustness during operation. Once the LN₂ tank is filled, the stage temperature can be maintained at cryogenic temperature for about 5 h. The cooling time is indeed longer than the few minutes obtained from the stimulations, and it is much shorter than the previous designs.

To heat the cold cryo-stage to room temperature, the liquid nitrogen in the tank is emptied and then compressed air is blown through the chimney to heat the cryo-stage. In less than 15 min, both the sample holder, the cold-finger, and the baseplate reach room temperature (Fig. 5b). The best SEM vacuum pressure is 2.5×10^{-5} mbar, and the pressure increased slightly during IPA sublimation, but the SEMs operation is not affected. The change in vacuum is negligible since the amount of organic ice is very low. The best vacuum recovers quickly for imaging after sublimation. To conclude, the new cryo-stage design is efficient in cooling and heating, reducing the IL processing time and increasing the throughput of the lithography process.

Because the different cryo-stage parts are made of different materials with different thermal expansion coefficients, we reasoned that the thermal stresses are most likely created during heating or cooling. The coefficient of thermal expansion of Cu, Al and PEEK are, respectively, 17×10^{-6} , 23×10^{-6} , and 5×10^{-5} per kelvin. For every kelvin in temperature difference, the PEEK pillars shrink 25 times more than Cu and Al parts. This will lead to thermal drift. Indeed, sample drift is observed while cooling the cryo-stage. However, this issue subsides once the temperature is stabilized.

The vibration of the cryo-stage is another factor that we observed due to boiling of the liquid nitrogen. The cryo-stage vibration is recorded by imaging the sharp edge of the Mo electrodes on the silicon substrate.

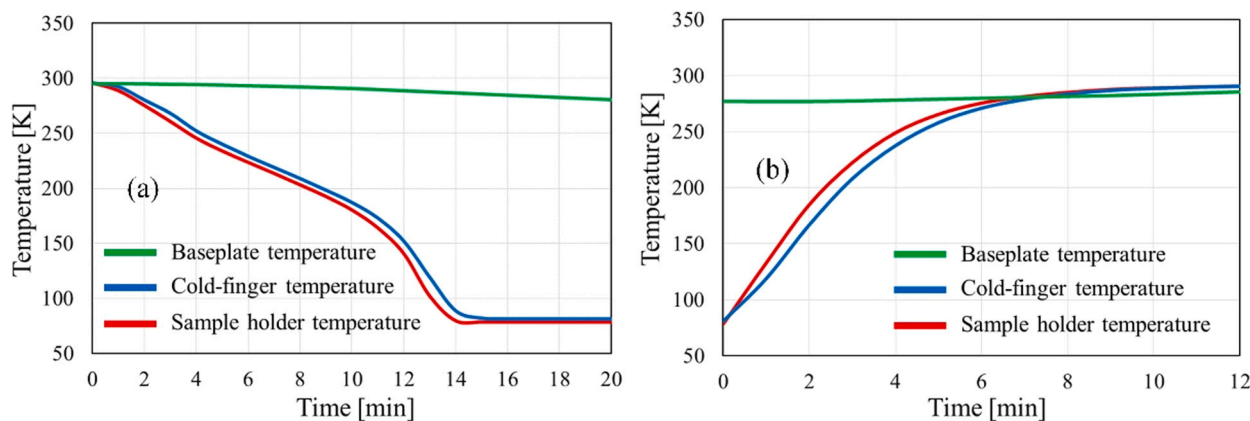


Fig. 5. Performance of the sample holder, cold-finger, and baseplate of the cryo-stage (a) cryogenic cooling using liquid nitrogen, and (b) heating up using compressed air.

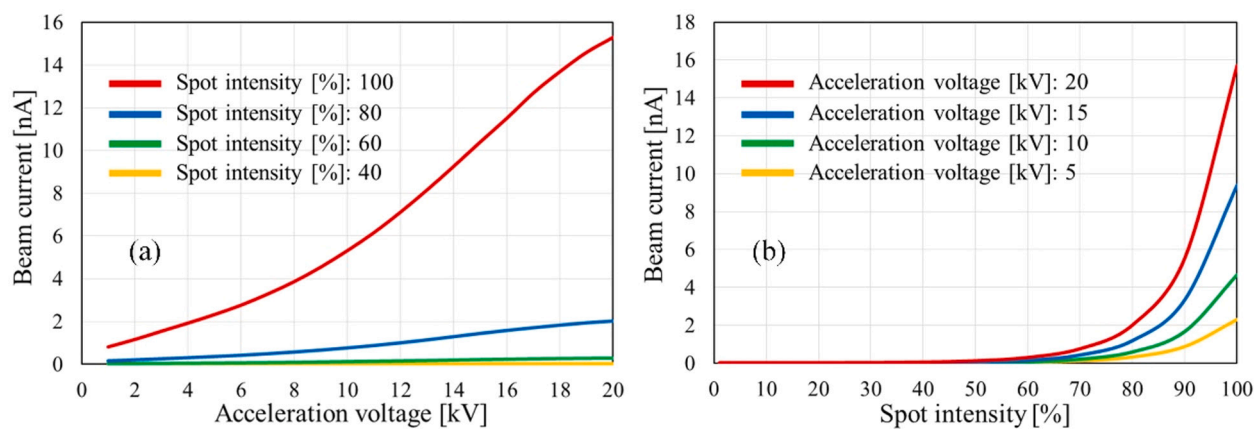


Fig. 6. E-beam current measurement using faraday cup connected to picoammeter with respect to e-beam (a) acceleration voltage for varying spot intensity, and (b) spot intensity for changing acceleration voltage.

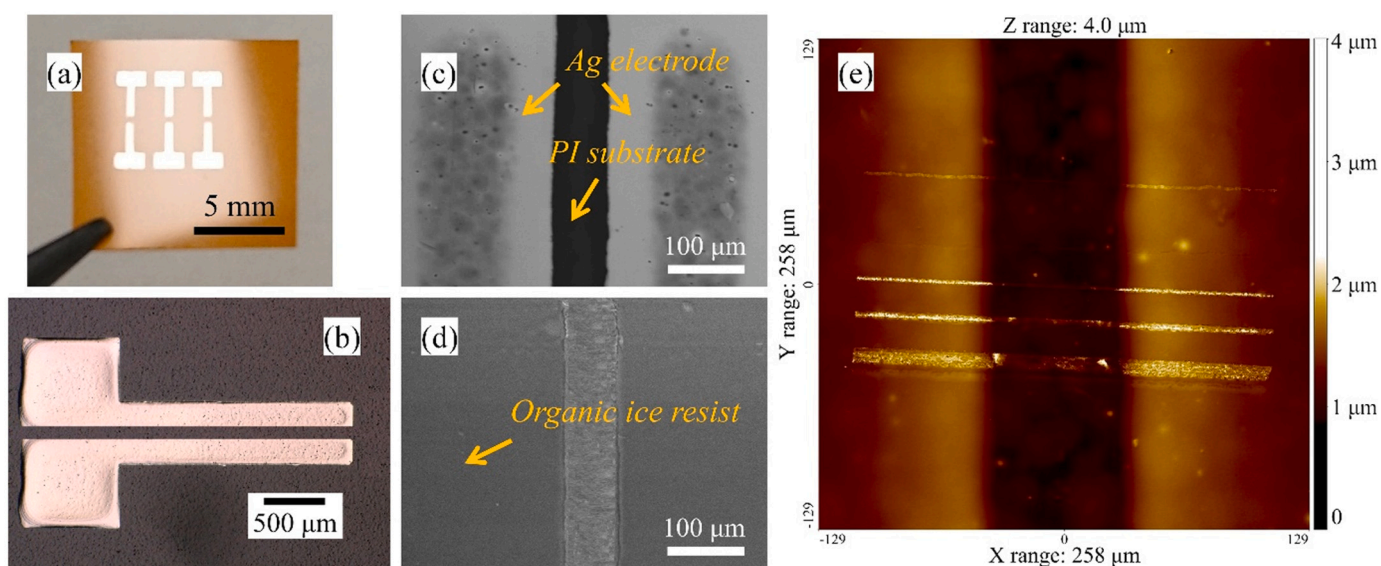


Fig. 7. (a) Photograph of the flexible PI substrate with inkjet-printed Ag electrodes, (b) optical micrograph of printed Ag electrode. SEM image of (c) pristine printed electronics transducers with Ag electrodes, (d) organic ice layer formation over the printed electronics transducers. And (e) 3D confocal micrograph of the cross-linked IPA organic ice resist pattern on flexible transducers.

Measurement reveals that the vibration of the cryo-stage is 180 ± 30 nm after the stable cryogenic temperature is reached. The integrated low magnetic field cartridge heater (HHP 50 W from SAN A/S) is used to control the cryo-stage temperature, and it does not affect the e-beam. As we expected, while in use, the heater causes the increase of LN₂ boiling and thus induces higher vibration. For example, the vibration of 2.1 ± 0.7 μm was recorded when the cryo-stage heated to 100 K.

Another important factor of ice lithography is the e-beam current measurement, which is linked with the electron dose process parameter. The Faraday cup, that remains at room temperature, is used for e-beam current measurement. Fig. 6 illustrates the e-beam current measurement for different e-beam acceleration voltage and spot intensity. The e-beam current increases with increasing acceleration voltage and spot intensity. These results correspond well with the SEM performance, such we can apply measured e-beam current data for IL with great confidence.

We also report a new IL application, where IL is combined with printed electronics transducers on flexible polyimide (PI) foil. There are several challenges associated with this application. (i) It is unclear if the insulating PI foil would cause significant sample charging that would prohibit e-beam processing, (ii) PI is also a good thermal insulator, and if

this would hinder ice layer formation, and (iii) whether the cooling of PI at the cryogenic temperatures would affect printed electronics devices. A set of carefully planned experiments were carried out to integrate printed electronics transducers and IL. The transducer consists of flexible 125 μm thick PI foil with inkjet printed silver electrodes (Fig. 7a, b). Inkjet printing was performed using silver nanoparticle-based ink (130-EG1) from PVnanocell employing Dimatix 2800-DMP inkjet printer with 10 pL cartridges from Fujifilm, and sintered at 150 °C for 30 min in thermal oven. The thickness of the inkjet printed silver electrodes are 800 ± 25 nm. Isopropanol (IPA) is used as precursor, because it is compatible with printed electronics devices. For a flat patterning surface, the flexible PI substrate was mounted on Si wafer using 'Apiezon N Grease'. This also ensured good thermal contact for the PI foil. Flexible transducers were mounted in the IL instrument and cooled down (Thermomechanical simulations showed that the PI foil cools down to 80 K within a minute following the cryo-stage), IPA vapor was injected through a nozzle placed above the cold substrate using gas injection system (GIS). Instant formation of IPA ice on the printed transducer was observed in the IL. Fig. 7 (c, d) shows SEM images of the printed electronics transducers before and after the condensation of IPA organic ice layer. Homogeneous ice layer covers the Ag electrodes and PI foil surface

in between. Rapid condensation forms amorphous or nanocrystalline ice thin films. Different primary electron (PE) energies were initially used to examine IPA ice layer to evaluate which e-beam energy would cause the least charging effects. For these printed electronic transducers, PE energies below 8 keV leads to significant charging such that SEM imaging and patterning was not possible. Thereafter, using a 10 keV PE energy and e-beam lithography system (Raith Elphy), lines were patterned across the silver electrodes applying line dose between 0.25 and 1 $\mu\text{C}/\text{cm}$, and area doses of 25 mC/cm^2 . The patterning took 17 min and 4 s. The uncross-linked IPA was sublimated by heating the cryo-stage and printed electronics device to room temperature. No degradation of the printed electronics transducers is observed, e.g., change of conductivity or delamination of inkjet-printed Ag electrodes. The cross-linked IPA patterns were then characterized using SEM and Olympus LEXT OLS4100 laser confocal microscope (Fig. 7e). The patterned IPA ice resist were between 1 μm and 10 μm wide, and the thickness of the cross-linked IPA line patterns varies between 150 nm and 650 nm depending on the electron doses. For IL performance please see our previous work, and here the smallest lines were just 4 nm wide [18].

4. Conclusion

We presented a new cryo-stage for ice lithography. The cryo-stage exhibits fast cooling and heating performance. The thermal stress remains well below the yield limit of the used materials. The cryo-stage design enables cryogenic cooling and warming up to room temperature in less than 20 and 15 min respectively, and thus increase the throughput the ice lithography process. Moreover, the IL patterning of IPA ice resist on flexible polyimide substrate with inkjet-printed silver electrode was also demonstrated. This confirms the compatibility of ice lithography process with flexible electronics technology, and thus IL can be utilized to develop printed electronic device with nanometer structures, sensors and actuators. This study shows several improvements in terms of key performance over the old cryo-stage design [27], which is summarized in Table 1. In the future, the cryo-stage design will be further modified and optimized to reduce stage vibration.

Declaration of competing interest

There are no known conflicts of interest associated with this publication.

Acknowledgment

The work presented in this article is supported by Lundbeck Foundation, grant R305-2018-2779 and Novo Nordisk Foundation, grant NNF0064289. We thank the support from the Marie and B. Richter's Foundation. RIH acknowledges that the research leading to these results has received funding from the European Union's Horizon 2020 research and innovation program under the Marie Skłodowska-Curie grant agreement no. 754462 (EuroTechPostdoc). We thank Hitachi High-Tech Europe, and DTU MEK and Nanolab workshops for technical support.

References

- [1] W. Wu, Inorganic nanomaterials for printed electronics: a review, *Nanoscale* 9 (2017) 7342–7372, <https://doi.org/10.1039/C7NR01604B>.
- [2] C. Ru, J. Luo, S. Xie, Y. Sun, A review of non-contact micro- and nano-printing technologies, *J. Micromech. Microeng.* 24 (2014), 053001, <https://doi.org/10.1088/0960-1317/24/5/053001>.
- [3] A. Kalkal, S. Kumar, P. Kumar, R. Pradhan, M. Willander, G. Packirisamy, S. Kumar, B.D. Malhotra, Recent advances in 3D printing technologies for wearable (bio)sensors, *Addit. Manuf.* 46 (2021), 102088, <https://doi.org/10.1016/j.addma.2021.102088>.
- [4] A.S. Dahiya, D. Shakthivel, Y. Kumaresan, A. Zumeit, A. Christou, R. Dahiya, High-performance printed electronics based on inorganic semiconducting nano to chip scale structures, *Nano Converg.* 7 (2020) 33, <https://doi.org/10.1186/s40580-020-00243-6>.
- [5] M.Y. Amarouch, J. El Hilaly, D. Mazouzi, AFM and FluidFM technologies: recent applications in molecular and cellular biology, *Scanning* 2018 (2018) 1–10, <https://doi.org/10.1155/2018/7801274>.
- [6] T. Zambelli, M.J. Aebbersold, P. Behr, H. Han, L. Hirt, V. Martinez, O. Guillaume-Gentil, J. Vörös, FluidFM: development of the instrument as well as its applications for 2D and 3D lithography, in: *Open-Space Microfluidics: Concepts, Implementations, Applications*, Wiley-VCH Verlag GmbH & Co. KGaA, Weinheim, Germany, 2018, pp. 295–323, <https://doi.org/10.1002/9783527696789.ch14>.
- [7] O. Guillaume-Gentil, M. Mittelviehhaus, L. Dorwling-Carter, T. Zambelli, J. A. Vorholt, FluidFM applications in single-cell biology, in: *Open-space Microfluidics: Concepts, Implementations, Applications*, Wiley-VCH Verlag GmbH & Co. KGaA, Weinheim, Germany, 2018, pp. 325–354, <https://doi.org/10.1002/9783527696789.ch15>.
- [8] Z. Faraji Rad, P.D. Prewett, G.J. Davies, High-resolution two-photon polymerization: the most versatile technique for the fabrication of microneedle arrays, *Microsyst. Nanoeng.* 7 (2021) 71, <https://doi.org/10.1038/s41378-021-00298-3>.
- [9] R. Momper, A.I. Landeta, L. Yang, H. Halim, H. Therien-Aubin, E. Bodenschatz, K. Landfester, A. Riedinger, Plasmonic and semiconductor nanoparticles interfere with stereolithographic 3D printing, *ACS Appl. Mater. Interfaces* 12 (2020) 50834–50843, <https://doi.org/10.1021/acsmi.0c14546>.
- [10] A.K. Nguyen, R.J. Narayan, Two-photon polymerization for biological applications, *Mater. Today* 20 (2017) 314–322, <https://doi.org/10.1016/j.matod.2017.06.004>.
- [11] Z. Huang, G. Chi-Pong Tsui, Y. Deng, C.-Y. Tang, Two-photon polymerization nanolithography technology for fabrication of stimulus-responsive micro/nanostructures for biomedical applications, *Nanotechnol. Rev.* 9 (2020) 1118–1136, <https://doi.org/10.1515/ntrev-2020-0073>.
- [12] H. Plank, R. Winkler, J. Sattelkow, J.D. Fowlkes, P.D. Rack, 3D Nanoprinting via focused electron beams, *Microsc. Microanal.* 24 (2018) 346–347, <https://doi.org/10.1017/S1431927618002222>.
- [13] H. Plank, R. Winkler, C.H. Schwalb, J. Hütner, J.D. Fowlkes, P.D. Rack, I. Utke, M. Huth, Focused electron beam-based 3D nanoprinting for scanning probe microscopy: a review, *Micromachines* 11 (2019) 48, <https://doi.org/10.3390/mi11010048>.
- [14] S. Barth, M. Huth, F. Jungwirth, Precursors for direct-write nanofabrication with electrons, *J. Mater. Chem. C* 8 (2020) 15884–15919, <https://doi.org/10.1039/D0TC03689G>.
- [15] J.M. De Teresa, A. Fernández-Pacheco, R. Córdoba, L. Serrano-Ramón, S. Sangiao, M.R. Ibarra, Review of magnetic nanostructures grown by focused electron beam induced deposition (FEBID), *J. Phys. D: Appl. Phys.* 49 (2016), 243003, <https://doi.org/10.1088/0022-3727/49/24/243003>.
- [16] Y. Hong, D. Zhao, D. Liu, B. Ma, G. Yao, Q. Li, A. Han, M. Qiu, Three-dimensional in situ electron-beam lithography using water ice, *Nano Lett.* 18 (2018) 5036–5041, <https://doi.org/10.1021/acs.nanolett.8b01857>.
- [17] D. Zhao, A. Han, M. Qiu, Ice lithography for 3D nanofabrication, *Sci. Bull.* 64 (2019) 865–871, <https://doi.org/10.1016/j.scib.2019.06.001>.
- [18] A. Elskova, A. Han, D. Zhao, M. Beleggia, Effect of molecular weight on the feature size in organic ice resists, *Nano Lett.* 18 (2018) 7576–7582, <https://doi.org/10.1021/acs.nanolett.8b03130>.
- [19] A. Han, J. Chervinsky, D. Branton, J.A. Golovchenko, An ice lithography instrument, *Rev. Sci. Instrum.* 82 (2011), 065110, <https://doi.org/10.1063/1.3601005>.
- [20] A. Han, A. Kuan, J. Golovchenko, D. Branton, Nanopatterning on nonplanar and fragile substrates with ice resists, *Nano Lett.* 12 (2012) 1018–1021, <https://doi.org/10.1021/nl204198w>.
- [21] W. Tiddi, A. Elskova, H.T. Le, P. Liu, M. Beleggia, A. Han, Organic ice resists, *Nano Lett.* 17 (2017) 7886–7891, <https://doi.org/10.1021/acs.nanolett.7b04190>.
- [22] A. Han, D. Vlassarev, J. Wang, J.A. Golovchenko, D. Branton, Ice lithography for nanodevices, *Nano Lett.* 10 (2010) 5056–5059, <https://doi.org/10.1021/nl1032815>.
- [23] Y. Hong, D. Zhao, D. Liu, G. Yao, M. Qiu, Development of an in-situ nanofabrication instrument for ice lithography, *Microelectron. Eng.* 224 (2020), 111251, <https://doi.org/10.1016/j.mee.2020.111251>.
- [24] Y. Hong, D. Zhao, J. Wang, J. Lu, G. Yao, D. Liu, H. Luo, Q. Li, M. Qiu, Solvent-free nanofabrication based on ice-assisted electron-beam lithography, *Nano Lett.* 20 (2020) 8841–8846, <https://doi.org/10.1021/acs.nanolett.0c03809>.
- [25] D. Zhao, B. Chang, M. Beleggia, Electron-beam patterning of vapor-deposited solid anisole, *ACS Appl. Mater. Interfaces* 12 (2020) 6436–6441, <https://doi.org/10.1021/acsmi.9b19778>.
- [26] G. Yao, D. Zhao, Y. Hong, S. Wu, D. Liu, M. Qiu, Direct electron-beam patterning of monolayer MoS₂ with ice, *Nanoscale* 12 (2020) 22473–22477, <https://doi.org/10.1039/D0NR05948J>.
- [27] W. Tiddi, A. Elskova, M. Beleggia, A. Han, Organic ice resists for 3D electron-beam processing: instrumentation and operation, *Microelectron. Eng.* 192 (2018) 38–43, <https://doi.org/10.1016/j.mee.2018.01.021>.
- [28] A. Han, D. Zhao, M. Qiu, Ice lithography, in: J.M.D. Teresa (Ed.), *Nanofabrication*, IOP Publishing, Bristol, UK, 2020, pp. 9–1 to 9–27, <https://iopscience.iop.org/book/978-0-7503-2608-7/chapter/bk978-0-7503-2608-7ch9>.
- [29] M. Huth, F. Porrati, O.V. Dobrovolskiy, Focused electron beam induced deposition meets materials science, *Microelectron. Eng.* 185–186 (2018) 9–28, <https://doi.org/10.1016/j.mee.2017.10.012>.
- [30] F. Porrati, M. Pohlitz, J. Müller, S. Barth, F. Biegger, C. Gspan, H. Plank, M. Huth, Direct writing of CoFe alloy nanostructures by focused electron beam induced deposition from a heteronuclear precursor, *Nanotechnology* 26 (2015), 475701, <https://doi.org/10.1088/0957-4484/26/47/475701>.

- [31] E. Villamor, F. Casanova, P.H.F. Trompenaars, J.J.L. Mulders, Embedded purification for electron beam induced Pt deposition using MeCpPtMe₃, *Nanotechnology* 26 (2015), 095303, <https://doi.org/10.1088/0957-4484/26/9/095303>.
- [32] H.T. Le, R.I. Haque, Z. Ouyang, S.W. Lee, S.I. Fried, D. Zhao, M. Qiu, A. Han, MEMS inductor fabrication and emerging applications in power electronics and neurotechnologies, *Microsyst Nanoeng.* 7 (2021) 59, <https://doi.org/10.1038/s41378-021-00275-w>.
- [33] R.G. Budynas, J.K. Nisbett, *Shigley's Mechanical Engineering Design*, 10th edition, McGraw-Hill, London, UK, 2010.